crystals

MDPI

Article

Precise Manipulation of Amino Groups in Zr-MOFs for Efficient Adsorption Performance

Qinghua Long, Yongqing Wang *, Ruiming Zhao, Tao Wang, Fanbing Lai, Xuebing Hu and Xiaojun Zeng *

School of Materials Science and Engineering, Jingdezhen Ceramic University, Jingdezhen 333403, China; L654391518@163.com (Q.L.); rmzhao163@163.com (R.Z.); L1436328003@163.com (T.W.); wangtaoky@sina.com (F.L.); xuebinghu2010@gmail.com (X.H.)

* Correspondence: wyq8248@126.com (Y.W.); zengxiaojun@jcu.edu.cn (X.Z.)

Abstract: Developing high-performance adsorbents for heavy metal (Cr (VI)) removal is essential for sustainable environments, but it is still challenging. Herein, a simple solvothermal method was proposed to fabricate Zr-MOFs (UiO-66), which was innovatively modified by amino groups to enhance the adsorption capacity of Cr (VI). The effects of the content of amino-functionalized ligands on the adsorption capacity and the influence of adsorbent content, solution pH, adsorption time, and adsorption temperature on the adsorption process were systematically investigated. Importantly, the pore structure and defect structure of UiO-66 can be finely regulated by adjusting the amino modification process. The adsorption process was fitted and analyzed using the kinetic model and the isotherm model. Impressively, the adsorption capacity of the amino-modified UiO-66 (UiO-66-NH_2) was greatly improved. These findings indicate that the surface functional group modification of MOFs is a promising method for adjusting their structure and improving their adsorption capacity.

Keywords: UiO-66-NH_2; amino group modification; fine regulation; defect structure; adsorption performance

Citation: Long, Q.; Wang, Y.; Zhao, R.; Wang, T.; Lai, F.; Hu, X.; Zeng, X. Precise Manipulation of Amino Groups in Zr-MOFs for Efficient Adsorption Performance. *Crystals* **2023**, *13*, 856. https://doi.org/10.3390/cryst13060856

Academic Editors: Yusuf Valentino Kaneti, Chaohai Wang and Ni Luh Wulan Septiani

Received: 24 April 2023
Revised: 17 May 2023
Accepted: 18 May 2023
Published: 23 May 2023

1. Introduction

Chromium (Cr) has different valence states, among which hexavalent chromium (Cr (VI)) is known as a class I carcinogen. Cr present in industrial wastewater has infiltrated into human living areas through the flow of aquatic systems, which indirectly affects human health and the economy. Therefore, the adsorption of Cr (VI) from industrial wastewater is of great significance. At present, finding an adsorbent that can highly efficiently treat Cr (VI) is one of the key issues in research. Metal–organic framework (MOF) is an emerging material, which is self-assembled by metal clusters and organic ligands through coordination bonds in a closed heating environment [1,2]. Because of their advantages, such as crystal structure designability, functional adjustability, and ultra-high specific surface area, MOF materials are widely utilized for adsorption [3–5], gas separation [6], oil–water separation [7], photocatalysis [8,9], and other fields [10–14]. Generally, when MOF materials are used as adsorbents, their adsorption performance is closely related to their pore and electrostatic interaction. However, the poor stability of most MOF materials in aqueous phase limits their application in water pollution treatment.

At the beginning of the 21st century, the University of Oslo, Norway developed a MOF material (UiO-66) [15]. It is a material with a $Zr_6O_4(OH)_4$ hexanuclear cluster as the central cluster, which is connected to 12 organic ligands terephthalic acid (BDC) through coordination bonds to form a $Zr_6O_4(OH)_4(BDC)_6$ structure. Compared with other MOF materials, UiO-66 has a better chemical stability, thermal stability, water stability, higher porosity, and richer unsaturated sites [16]. This means that the UiO-66 series of materials can be well applied in the field of wastewater treatment. However, UiO-66, with its "perfect" crystal structure (defect free) (Figure 1) has a strong binding energy between the metal

clusters and the connectors, which will significantly prevent other guest molecules from contacting with Zr active sites, resulting in a poor adsorption performance.

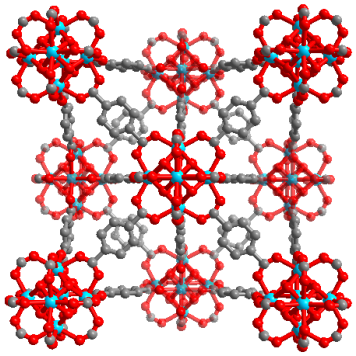

Figure 1. Scheme illustrating the "perfect" UiO-66 crystal structure.

Recently, scholars have successfully synthesized materials with better adsorption performance through functional ligand regulation strategies. For example, Zhang et al. [17] explored the effect of carboxyl introduction on adsorption performance by changing the molar ratio of H_2BDC to H_2BDC-COOH. The BET specific surface areas of UiO-66-COOH-1, UiO-66-COOH-2, and UiO-66-COOH-3 were 1340.6, 1016.3, and 828.2 $m^2 \cdot g^{-1}$, respectively. Since the adsorption capacity of the cationic organic dye, methylene blue, depends on the combined effects of electrostatic interaction and active sites, the results show that UiO-66-COOH-2 has a better adsorption effect. Xie et al. [18] studied the effect of -OH on the photocatalytic reduction in Cr (VI) by regulating -OH functional groups. The results showed that under visible light conditions, the maximum equilibrium removal rate of UiO-66-$(OH)_2$ was about 90%, which was significantly stronger than that of UiO-66-OH with a removal rate of 45%, indicating that the introduction of -OH can increase the photocurrent density and improve the inhibition of electron–hole recombination during photocatalysis.

In this work, the UiO-66 series materials were prepared by the solvothermal method. By adjusting the amount of benzoic acid in order to adjust the defects in the crystal structure, UiO-66 powder with a high crystallinity and high yield was synthesized. By introducing amino functional groups on the surface of UiO-66 to finely regulate the size, microstructure, pores, and defects of UiO-66, the effects of solution pH, initial concentration, adsorption temperature, and adsorption time on the adsorption process were investigated, and the adsorption mechanism of UiO-66-NH_2 was revealed.

2. Experiment

2.1. Material

Zirconium chloride ($ZrCl_4$), terephthalic acid, 2-amino terephthalic acid ($C_8H_7NO_4$), benzoic acid, DMF, anhydrous methanol (CH_3OH), and potassium dichromate ($K_2Cr_2O_7$) were purchased from China National Medicines Corporation Ltd., Shanghai, China. All reagents were AR fractionated, and no further purification was required during use.

2.2. Synthesis of Compounds

UiO-66 was synthesized by the solvothermal method. $ZrCl_4$ (0.70 mmol) and p-phthalic acid (H_2BDC, 0.70 mmol) were added to a beaker containing 20 mL of DMF, treated in an ultrasound machine for 10 min, then, DMF (20 mL) and benzoic acid (4.274 g) was added. Then, the mixture was ultrasonically treated for 20 min until it was completely dissolved, then transferred to a PTFE lining. Placed in an oven, and to react at 120 °C for 24 h. After the reactor was cooled to room temperature, the inner lining was taken out, and the solution was centrifuged to obtain a white powder, which was washed with DMF and CH_3OH for more than three times individually, and placed in 80 °C vacuum drying for 48 h. The final product was labeled as UiO-66. UiO-66-NH_2 was replaced with

2-aminoterephthalic acid (NH_2BDC), which was labeled as U-N-x (x = 0.5, 1, 2, 4 when x = 1, $n_{(NH2BDC)}$ = 0.70 mmol), according to the amino-functionalized ligand content; the remaining steps were consistent with the preparation process of UiO-66.

2.3. Characterization

The crystal structures of the materials were investigated by X-ray diffractometer (XRD, DX-2700B; Dandong Haoyuan Instrument Co., Ltd., Dandong, China), and XRD spectra were acquired within a scanning range (2θ) from 5 to 80. The crystal morphology of the UiO-66 was observed through a scanning electron microscope (SEM, SU8010; Hitachi Ltd., Tokyo, Japan). The specific surface areas were determined using the standard multi-point techniques of N_2 adsorption (Micromeritics ASAP 2020; Micromeritics Instrument Corporation, Norcross, GA, USA) and measured by adsorption–desorption at 77 K. The functional groups present on the surface of the adsorbent were analyzed using Fourier transform infrared spectroscopy (FTIR, Nicolet 5700; Thermo Nicolet Corporation, Waltham, MA, USA). The surface atomic state of the adsorbent was analyzed using X-ray photoelectron spectroscopy (XPS, Escalab 250Xi; Thermo Fisher Scientific, Waltham, MA, USA). DTA-TG curves of the samples were recorded using a thermal analyzer (NETZSCH STA 449C, Selb; NETZSCH-Gerätebau GmbH, Selb, Germany).

2.4. Adsorption Experiment

Potassium dichromate ($K_2Cr_2O_7$, 373.5 mg) was dissolved in 100 mL deionized water to prepare a Cr (VI) solution with a concentration of 1000 $mg{\cdot}L^{-1}$. Solutions of other concentrations were obtained by diluting the stock solution. Adsorbent and 50 mL Cr (VI) solution were added to a conical flask and stirred at a fixed temperature in a magnetic thermostatic water bath. After adsorption, the supernatant was separated from the mixture by centrifugation. The absorbance of the supernatant after centrifugation was determined by diphenyl carbazide spectrophotometry at 540 nm wavelength, and the concentration after adsorption was measured. The effects of pH (2–10), adsorbent dose (10–30 mg), adsorption time (0–34 h), adsorption temperature (293–313 K), initial concentration (10–300 $mg{\cdot}L^{-1}$), and functional group content on adsorption performance were investigated.

The unit adsorption capacity and removal rate are shown in Equations (1) and (2):

$$q_e = \frac{(C_0 - C)*V}{m} \quad (1)$$

$$w = \frac{(C_0 - C)}{C_0} \times 100\% \quad (2)$$

where q_e ($mg{\cdot}g^{-1}$) is the unit adsorption amount; m (g) is the mass of the adsorbent; V(L) is the volume of the Cr (VI) solution; w is the removal rate; C_0 ($mg{\cdot}L^{-1}$) and C ($mg{\cdot}L^{-1}$) represent the concentration of the adsorbate before and after adsorption, respectively.

2.5. Chromium Stability

UiO-66-NH_2 was placed in a conical flask containing 50 mL of Cr (VI) solution (300 $mg{\cdot}L^{-1}$), then, stirred in a 303K thermostat water bath for 48 h. The precipitate was centrifuged and washed with deionized water and dried. The chromium-loaded UiO-66-NH_2 was placed in beakers containing 0.01 $mol{\cdot}L^{-1}$ sulfuric acid, nitric acid, hydrochloric acid, and sodium hydroxide solution, respectively. Meanwhile, the chromium stability of the material in acidic and alkaline aqueous systems was studied by stirring and ultrasound.

3. Results and Discussion

3.1. Effect of the Regulator Concentration on Synthetic UiO-66

The concentration of the regulator will affect the crystal structure and morphology [19]. The effect of benzoic acid content on the crystal structure and yield of UiO-66 was studied. Combined with XRD patterns and yield (Figure 2), it can be concluded that the addition of benzoic acid has no effect on the crystal structure of UiO-66. With the increase in its content, the yield increased first and then decreased. When the content was greater than 50 equivalents (based on $ZrCl_4$), the yield decreased significantly, and the yield was less than 0.001 g after reaching 100 equivalents content. This may be because the increase in benzoic acid strengthens its competition for zirconium oxygen coordination, resulting in a higher concentration of connector defects [19–21]. The intermediate formed between benzoic acid and zirconium oxygen ions is not conducive to nucleation, which will hinder nucleation, and the crystal core growth rate thus growing into larger crystals [19,22]. In the subsequent experiments, the regulator in the adsorbent was 50 equivalents of benzoic acid.

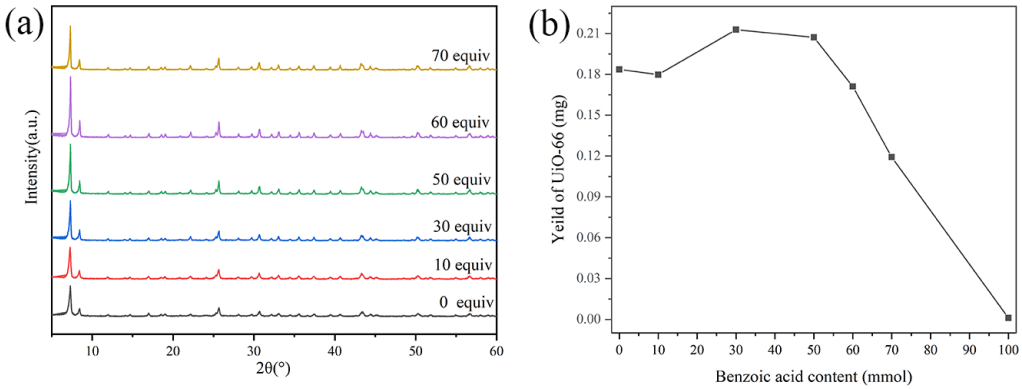

Figure 2. XRD patterns (**a**) and yield (**b**) of UiO-66.

3.2. Structural and Pore Regulation of UiO-66-NH_2

The above UiO-66 with 50 equivalents of benzoic acid was used to adsorb 100 mg·L^{-1} Cr (VI) solution, the unit adsorption capacity was 45 mg·g^{-1}, and the removal rate was 23%. It can be preliminarily inferred that 23% of Cr (VI) adsorption originated from the adsorption site. Zhang [23] used UiO-66-NH_2 to remove 100 mg·L^{-1} Cr (VI) solution, and obtained q_m of 252 mg·g^{-1} using the Langmuir model. Based on this, the ligand of UiO-66 was replaced with 2-amino terephthalic acid containing an amino functional group. The effects of amino-functionalized ligand content on the crystal structure, pore structure, and adsorption capacity were studied. Then, the U-N-x with the best performance and adsorption capacity was selected for studying the best adsorption conditions, including the adsorbent content, solution pH, adsorption time, adsorption temperature, and initial concentration. Finally, the adsorption mechanism was discussed.

This section gives some basic information about the U-N-x. Figures 3a–c and 4a–e show that the effect of amino-functionalized ligand content (x = 0, 0.5, 1, 2, and 4) on the crystal structure and morphological characteristics. As can be seen from the SEM images, when $x < 1$, the crystal morphology is approximately spherical and there is no distinctly octahedral edge, and the addition of amino groups increased grain size. When $x \geq 1$, the crystals have an obviously octahedral structure with sharp edges and corners. With the increase in ligand content, the crystal size is enlarged, and the octahedral edge is more evident. Figures 3a and 4a show the XRD patterns of U-N-x. Obviously, ligand regulation has no significant effect on the crystal structure of the synthesized UiO-66-NH_2. This may be because with the increases in ligand content, enough ligands make up for the defects caused by acid regulation [21], indirectly protecting the growth of crystal nucleus. However, since the content of the metal source is determined, the color of the residual liquid shows that there are more residual ligands after synthesis. Clearly, the morphology

characterization can show that the introduction of amino groups effectively regulates the microstructure of UiO-66.

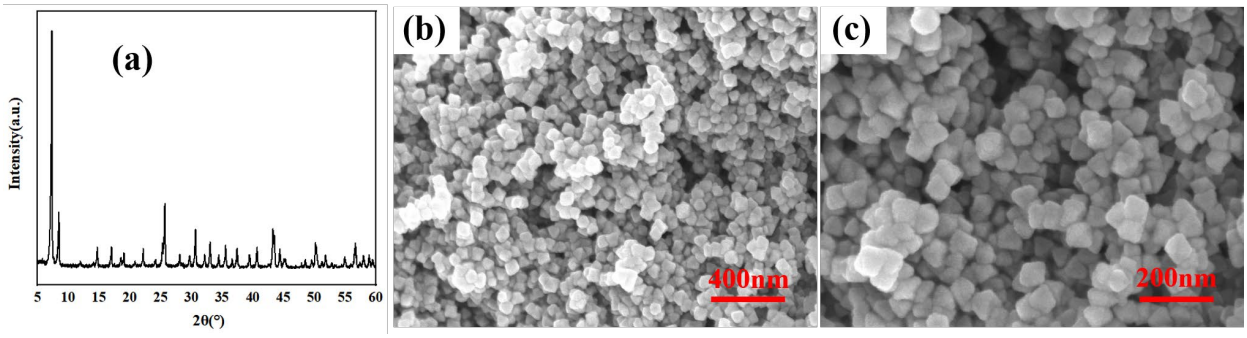

Figure 3. (**a**) XRD patterns and (**b**,**c**) SEM images of U-N-0.

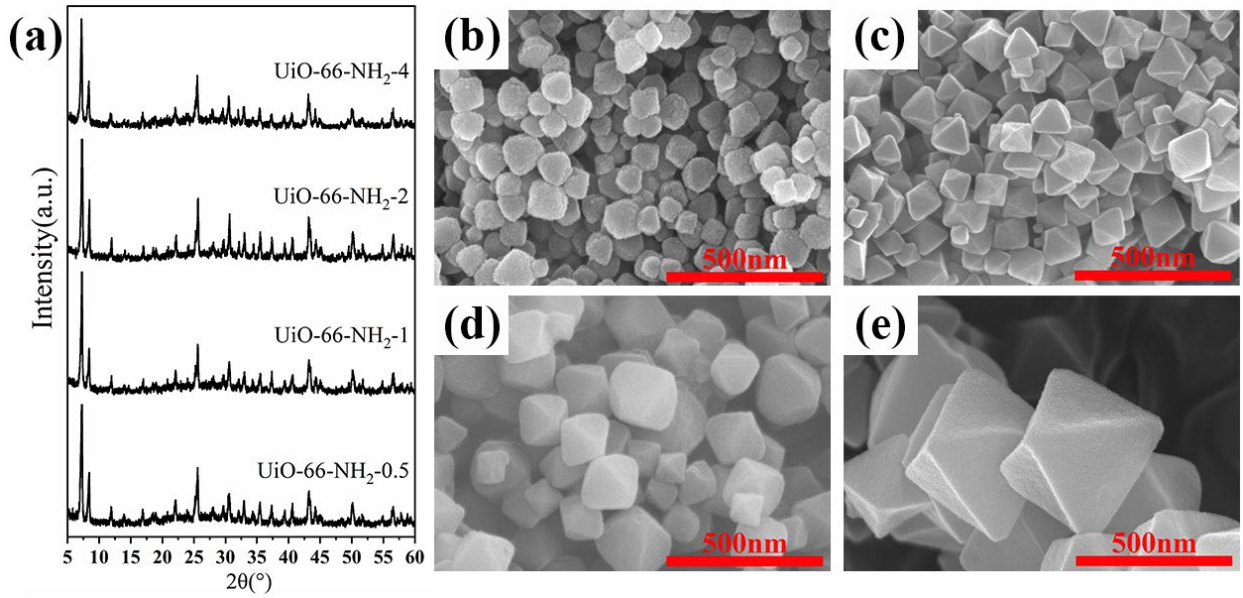

Figure 4. (**a**) XRD patterns and SEM images of (**b**) U-N-0.5, (**c**) U-N-1, (**d**) U-N-2, and (**e**) U-N-4.

Figure 5 shows the DTA-TG curves of U-N-x; the introduction of an amino group will reduce the thermal stability of the material. The pyrolysis process of materials is mainly divided into the loss of guest molecules and the collapse of inorganic–organic frameworks. Compared with the UiO-66 material that began to collapse at 500 °C, UiO-66-NH_2 series materials collapsed at about 400 °C due to the oxidability and high activity of the amino group. Since the loss of guest molecules cannot be accurately defined stoichiometrically, defect-quantified analysis was performed on the ligands lost by MOFs after dehydroxylation. The structural formula of UiO-66-NH_2 is $Zr_6O_6(NH_2BDC)_6$, that is, the percentage of ligand loss should be 60% theoretically. Assuming that the final residual amount is ZrO_2 at 800 °C, it can be calculated that during the period of 373 °C~800 °C, when x = 1, the ligand loss percentage of U-N-1 is the least, 39%, that is, the most linker defects.

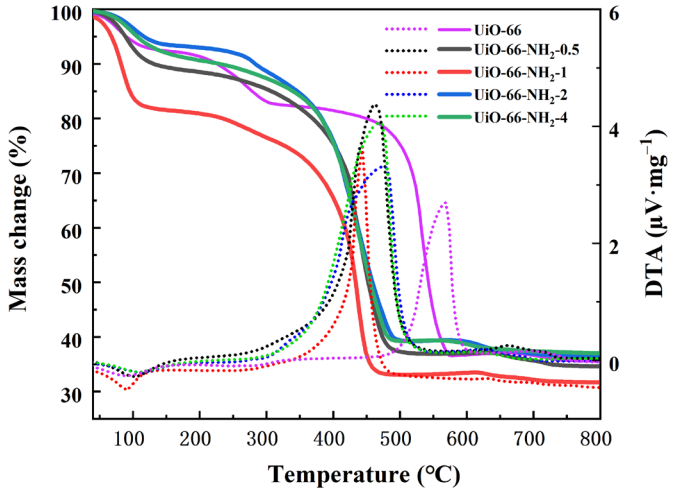

Figure 5. DTA-TG curve of U-N-x (x = 0, 0.5, 1, 2, 4).

The nitrogen adsorption–desorption isotherm of U-N-x are shown in Figure 6a,b, where the maximum Langmuir specific surface area of U-N-1 is 1420.9 mg·g^{-1}, and the minimum specific surface area of U-N-4 is 1069.5 mg g^{-1}, as shown in Table 1. According to the isotherm and pore size distribution diagram, it can be found that with the increase in ligand content, the micropores' content decreases, and the mesopores and macropores content increases, indicating that the amino ligand content has a great influence on the specific surface area and pore size of the material. The results confirmed that the introduction of amino groups effectively regulated the specific surface area and pore structure of UiO-66.

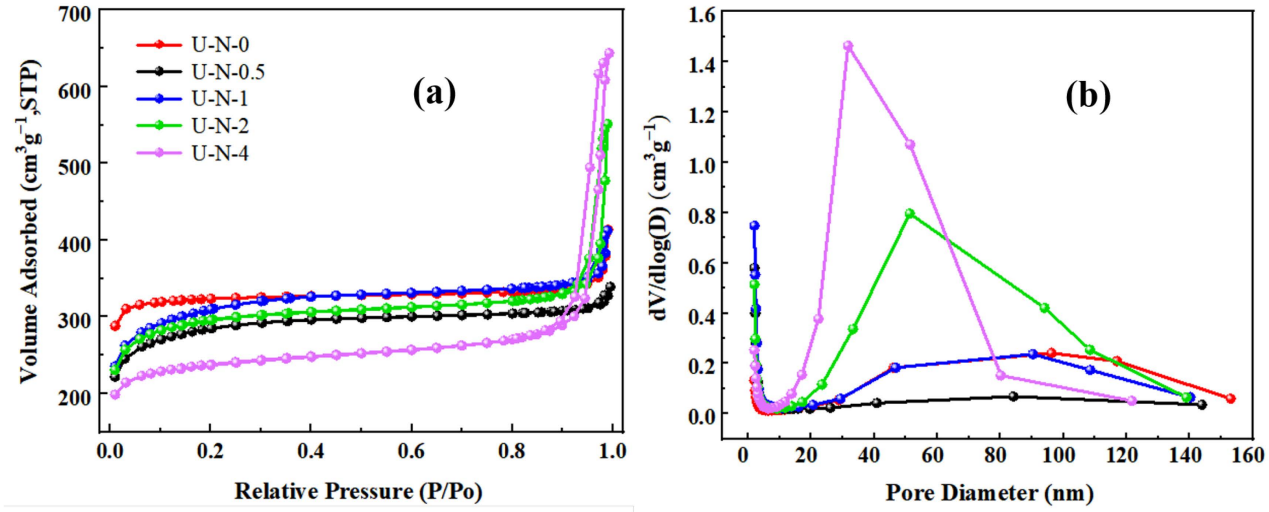

Figure 6. (**a**) Nitrogen adsorption–desorption isotherms and (**b**) pore diameter distributions of U-N-0, U-N-0.5, U-N-1, U-N-2, and U-N-4 sample.

Table 1. The BET fitted data for U-N-x.

MOFs	Specific Surface Area ($m^2 \cdot g^{-1}$)	Pore Size (nm)	Pore Volume ($cm^3 \cdot g^{-1}$)
U-N-0	1423.04	3.5	0.52
U-N-0.5	1297.85	2.01	0.49
U-N-1	1420.89	2.09	0.55
U-N-2	1345.18	2.31	0.58
U-N-4	1069.46	3.58	0.72

3.3. Stability of U-N-x

Excellent chemical stability in various water environments is the basis for the better application of materials in water treatment. In this part, the chemical stability of U-N-1 in common acid-base reagents was investigated by analyzing the changes in crystal structure and morphology before and after corrosion. From Figure 7a–e, it can be seen that the adsorbent can basically resist the corrosion of acid and alkali reagents and maintain the crystal structure and the octahedral crystal morphology. It can be seen that UiO-66-NH_2 has good chemical stability.

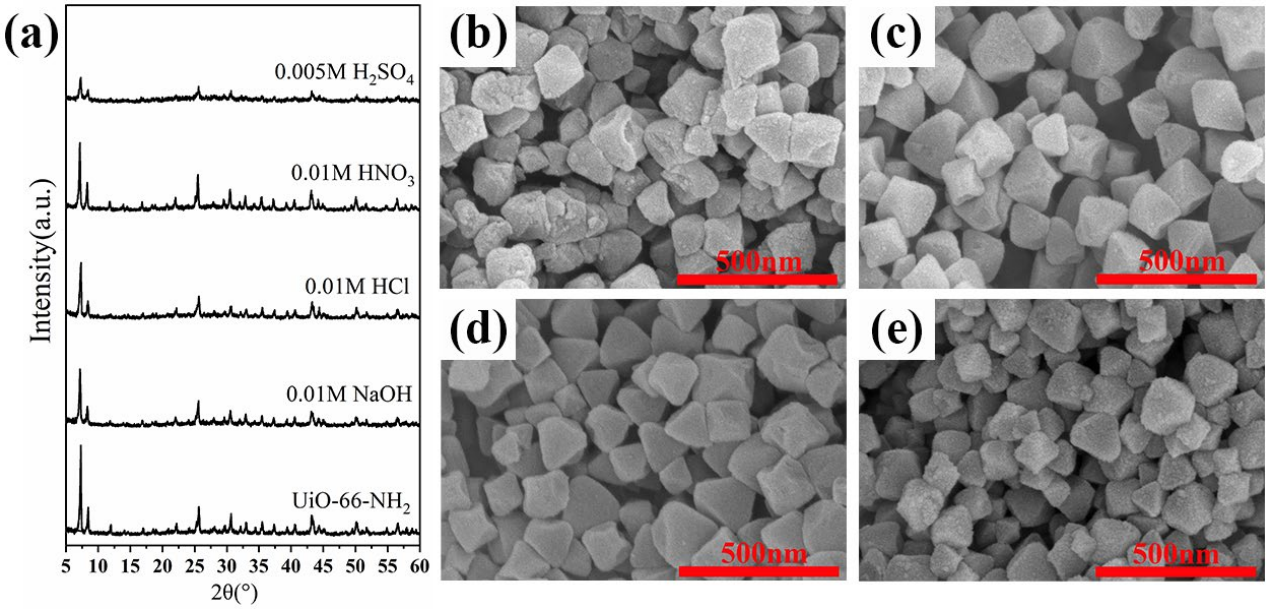

Figure 7. (**a**) XRD patterns of adsorbent that corroded by different pH solutions. SEM images of corrosion by (**b**) H_2SO_4, (**c**) HNO_3, (**d**) HCl, and (**e**) NaOH.

3.4. Adsorption Performance of UiO-66-NH_2

In order to study the effect of the functional group regulation on the adsorption capacity, 10 mg U-N-x was added to a beaker containing 50 mL Cr (VI) (100 mg·L^{-1}) solution for adsorption. As shown in Figure 8a, the adsorption capacity increased first and then decreased with the increase in amino ligand content. When x = 1, the unit adsorption rate reached a maximum of 305.16 mg·g^{-1}. Furthermore, the variation in adsorption capacity and removal rate were studied when the adsorbent was 10, 20 and 30 mg and stirred at a constant temperature for 4 h. It can be seen from Figure 8b that with the increase in adsorbent content, the adsorption capacity decreased and the removal rate decreases. This is because the increase in the adsorbent in the system can bring a more active site, thereby capturing more Cr (VI) ions. With the increase in adsorbent dosage, the particles accumulate, resulting in a decrease in removal efficiency. Considering the effective utilization rate of the adsorbent and the removal efficiency of Cr (VI), U-N-1 was selected as the adsorbent for subsequent research, and the mass of the adsorbent was 10 mg.

In adsorption application, the solution pH can affect the adsorption capacity for UiO-66-NH_2 to Cr (VI) by affecting the existence form of the adsorbate and the surface property of the adsorbent. Therefore, the effect of solution pH on the adsorption process was investigated. The pH of the solution was adjusted by adding 0.1 mol·L^{-1} nitric acid or 0.1 mol·L^{-1} sodium hydroxide. The initial concentration of Cr (VI) was 10 mg·L^{-1}, the adsorption temperature was 303 K, the adsorption time was 1 h, and the adsorbent content was 10 mg. As shown in Figure 9, the adsorption capacity of Cr (VI) decreased gradually with the increase in pH from 2 to 10. In the solution of pH = 1–6, Cr (VI) mainly exists in the form of $HCrO^{4-}$ and $Cr_2O_7^{2-}$. The amino group (-NH-/-NH_2) on the surface of the adsorbent is protonated, and adsorbs Cr (VI) anions through electrostatic attraction. The

adsorption capacity increased with the increase in acidity. Therefore, when the solution pH increases from 2, the removal rate of Cr (VI) gradually decreases. When the pH was 2, the adsorption capacity was 15.76 $mg \cdot g^{-1}$, reaching the maximum value. With the increase in pH, the negative charge on the surface of U-N-1 nanoparticles also increased, leading to an increase in the repulsive force between Cr (VI) and MOF nanoparticles [24]. In addition, OH^- in aqueous solution will also compete for adsorption sites, resulting in a gradual weakening of the adsorption. This indicates that the main driving force for adsorption of Cr (VI) is electrostatic attraction.

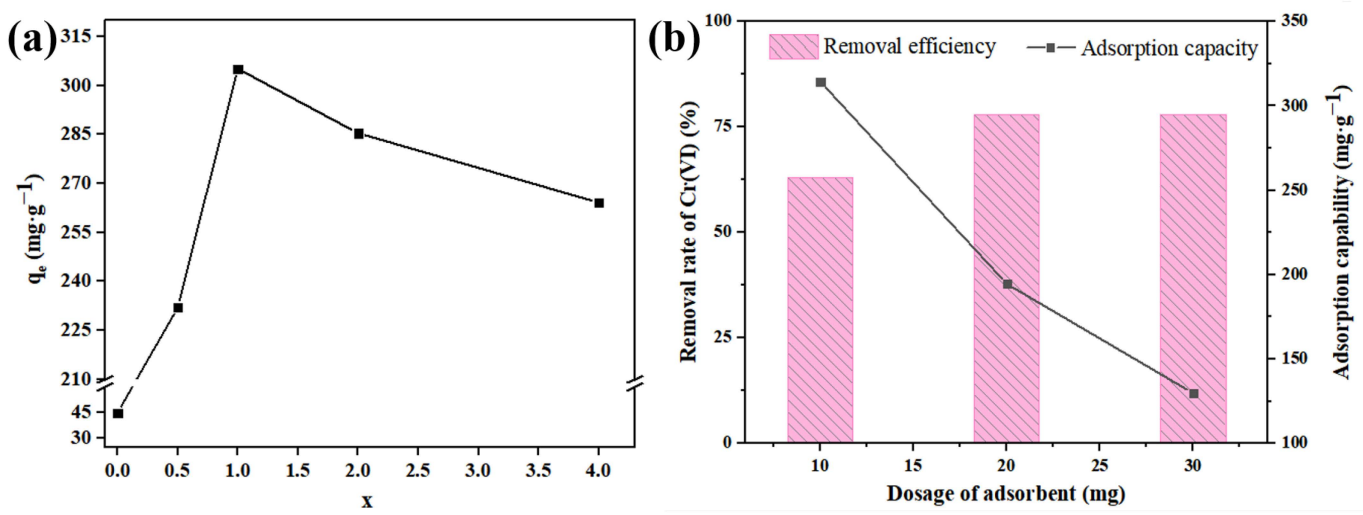

Figure 8. (**a**) Effect of amino ligand concentration on the adsorption amount of Cr (VI). (**b**) Effect of adsorbent content on adsorption capacity.

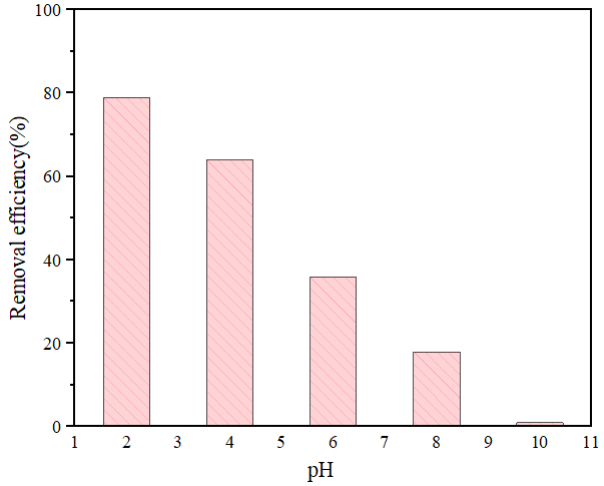

Figure 9. The removal efficiency of UiO-66-NH_2 to Cr (VI) at different pH values.

3.5. Structural Characterization before and after Adsorption Measurement

Figure 10a and b show the structural stability of the material before and after adsorption. It can be seen that the morphology before and after adsorption did not change significantly, but the XRD pattern changed considerably. Although the structure of the main peak has not changed, it was evident that there are many heterogeneous peaks in the diffraction peaks of UiO-66-NH_2 loaded with Cr (VI), and the peak intensity is significantly reduced, which may be due to the reduction in diffraction intensity and the broadening of diffraction peaks caused by Cr (VI) as an exotic substance.

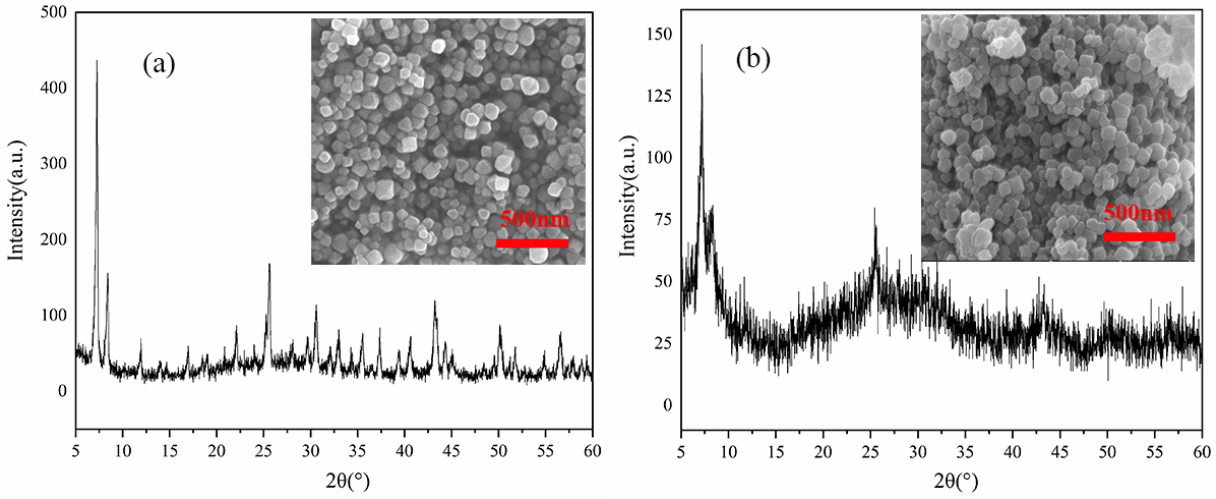

Figure 10. XRD patterns and SEM images (**a**) before and (**b**) after adsorption measurement.

The FTIR analysis of UiO-66-NH_2 samples before and after adsorption was performed to determine the specific effect of functional groups in UiO-66-NH_2 on Cr (VI) adsorption, as shown in Figure 11. The wider peak at ~3420 cm^{-1} is the N-H stretching vibration region, and the absorption band at ~1560 cm^{-1} is mainly the vibration of the benzene ring skeleton [25]. The absorption band of the sample after adsorption is affected by Cr (VI) and has a certain offset. The absorption peaks at 1430 and 1370 cm^{-1} are C-O bond stretching vibrations, while the absorption peak observed at 1260 cm^{-1} is the characteristic peaks of C-N bond in aromatic amines [26], and the absorption peak at 660 cm^{-1} is attributed to the vibrations of Zr-O [27]. After loading the Cr element in UiO-66-NH_2 material, a new small peak can be clearly seen at 721 cm^{-1}, corresponding to the vibration of the Cr-O bond [28,29], which indicates that Cr (VI) is successfully adsorbed. In addition, the intensity of the UiO-66-NH_2-Cr (VI) peak at 1260 cm^{-1} is significantly reduced, which means that the -NH_2/-NH_3^+ on the surface of UiO-66-NH_2 may have participated in the adsorption process, so this process may be related to electrostatic attraction [30]. The FTIR analysis showed that Cr (VI) was successfully captured, and this process may be achieved by electrostatic attraction.

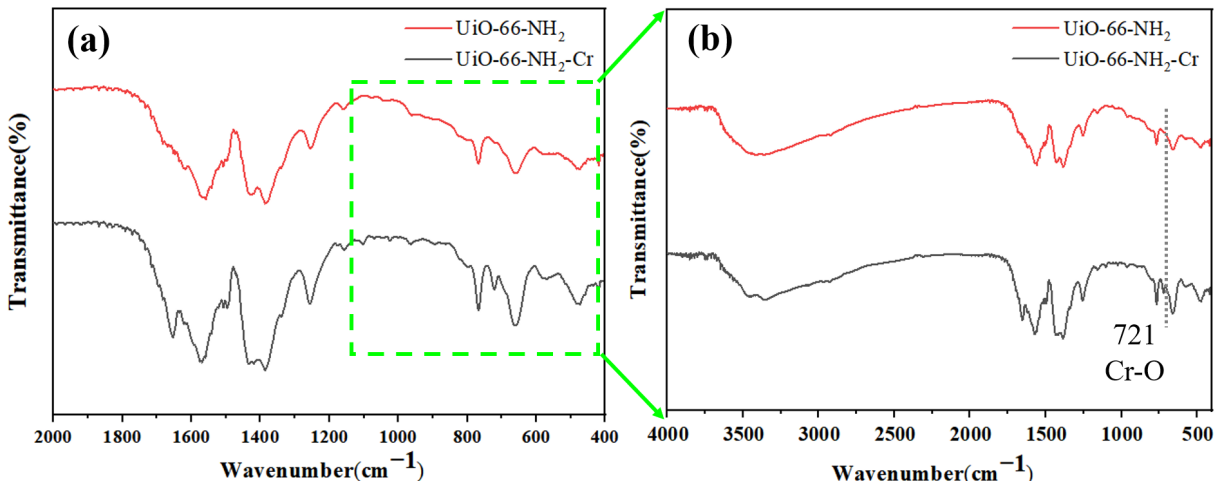

Figure 11. (**a**) FTIR wide-scan spectrum and (**b**) local FTIR spectrum before and after adsorption measurement.

3.6. Adsorption Kinetics

The influence of the adsorption time on the adsorption capacity of Cr (VI) concentration at different time points. The initial concentration of Cr (VI) solution was 100 mg·L^{-1}, and the solution volume was 150 mL. The adsorbent content was set to 10 mg, the adsorption temperature was 303 K, and the solution pH was 2. As shown in Figure 12a, the adsorption capacity of U-N-1 for Cr (VI) gradually increased and reached adsorption equilibrium within about 2040 min. The rapid removal rate at the initial stage of adsorption can be attributed to a large number of empty adsorption sites. With the increase in adsorption time, the concentration of available empty adsorption sites gradually decreases, and the adsorption sites were blocked by Cr (VI) molecules, resulting in an increase in adsorption capacity and a gradual decrease in adsorption rate.

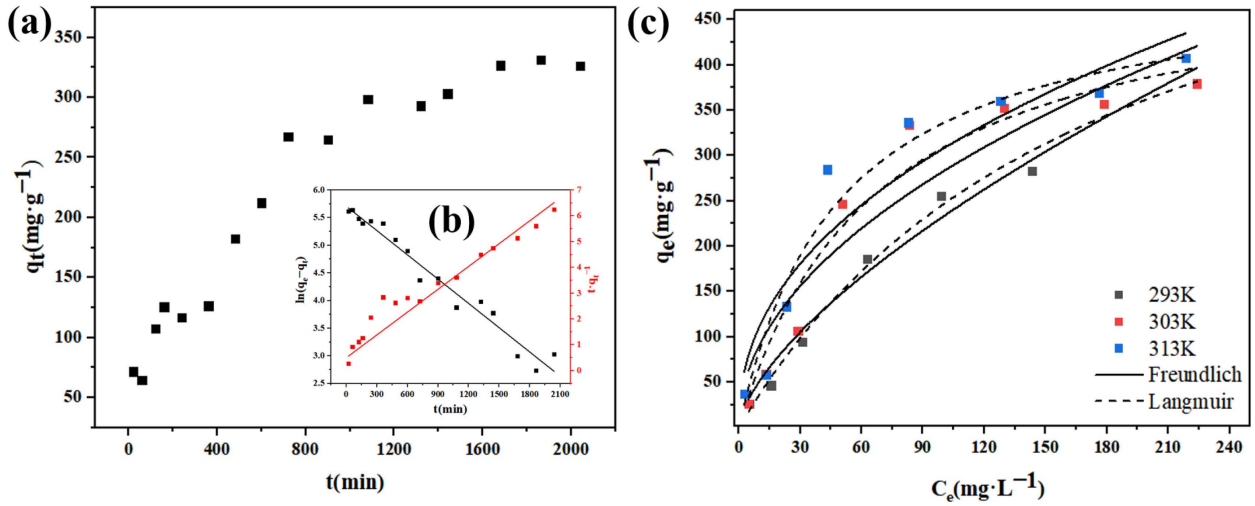

Figure 12. (**a**) Adsorption kinetic at U-N-1 to Cr (VI). Pseudo-first-order (black of (**b**)) and pseudo-second-order (red line of (**b**)) kinetic models. (**c**) Adsorption isotherms of U-N-1 to Cr (VI).

The pseudo-first-order and pseudo-second-order kinetic models are often used to evaluate the adsorption rate and kinetic mechanism. The fitting curve of the kinetic model is shown in Figure 12b, and the kinetic fitting equation and adsorption-related kinetic parameters are shown in Table 2, where q_e (mg·g^{-1}) and q_t (mg·g^{-1}) are the equilibrium adsorption capacity and the adsorption capacity at the time t, respectively. $Q_{e(cal)}$ (mg·g^{-1}) is the adsorption saturation, and k_1 (min^{-1}) and k_2 (g·(mg·min)$^{-1}$) are the pseudo-first-order and pseudo-second-order rate constants, respectively.

Table 2. Kinetic fitting parameters.

Model	Equation	Parameter	$q_{e(cal)}$ (mg·g^{-1})	R^2
Pseudo-first-order	$\ln(q_e - q_t) = \ln q_e - \frac{k_1 t}{2.303}$	k_1 = 0.00146	300.88	0.9662
Pseudo-first-order	$\frac{t}{q_t} = \frac{t}{q_e} + \frac{1}{k_2 q_e^2}$	k_2 = 0.00000858	370.37	0.9885

It can be seen from Table 2 that the correlation coefficient R^2 of the pseudo-second-order kinetic model is higher than 0.98, which is significantly higher than the pseudo-first-order kinetic model. In addition, compared with the experimental q_e (346.96) value, the q_e value calculated by the pseudo-second-order kinetic model is closer to the q_e value calculated by the pseudo-first-order kinetic model. Therefore, the pseudo-second-order kinetic model is more suitable for explaining the adsorption process of Cr (VI) by nanocrystals U-N-1, indicating that the adsorption process is mainly chemical adsorption.

3.7. Adsorption Isotherms

To explore the influence of adsorption temperature and initial concentration of solution on adsorption, the adsorption capacity of 10 mg adsorbent at different concentrations from 10 mg·L^{-1} to 300 mg·L^{-1} was studied at 293 K, 303 K, and 313 K, and the adsorption isotherm was plotted. The results are shown in Figure 12c. To study the adsorption capacity of U-N-1, the Langmuir model and the Freundlich model were used to fit the experimental data. The fitting results are shown in Table 2. The Langmuir model is usually used to fit the monolayer adsorption process on a homogeneous surface [31]. In contrast, the Freundlich model is often used as an empirical adsorption formula to summarize some experimental facts. The expressions of these two models are as follows:

$$q_e = \frac{q_m K_L C_e}{1 + K_L C_e} \quad (3)$$

$$q_e = K_F C_e^{\frac{1}{n}} \quad (4)$$

Among them, q_e (mg·g^{-1}) and q_m (mg·g^{-1}) are the equilibrium adsorption capacity and saturated adsorption capacity, respectively. C_e (mg·L^{-1}) is the equilibrium concentration of the solution. K_L (L·mg^{-1}) is an adsorption constant related to the adsorption energy of the binding site, which represents the adsorption enthalpy, and is related to temperature. K_F and n are Freundlich constants related to the adsorption capacity and adsorption strength, respectively.

According to the results in Table 3, the K_L values at different temperatures are far less than 1, indicating that there is a strong interaction between U-N-1 and Cr (VI). Comparing the R^2 values of the two models, it can be seen that the R^2 value fitted by the Langmuir model is greater than 0.94, indicating that Langmuir model can better describe the adsorption process of U-N-1 for Cr (VI). These results show that the adsorbent is mainly monolayer adsorption during the adsorption process.

Table 3. Isotherm fitting parameters.

Temperature (K)	Langmuir Model			Freundlich Model		
	q_m (mg·g^{-1})	K_L (L·mg^{-1})	R^2	K_F (L·mg^{-1})	n	R^2
298	610.230	0.00754	0.9414	16.212	1.691	0.922
308	515.094	0.01496	0.9479	29.193	2.029	0.874
318	500.451	0.0204	0.9492	40.144	2.261	0.882

3.8. Adsorption Mechanism

The adsorption mechanism was analyzed by XPS, and the results are shown in Figure 13. Compared with the total spectrum of UiO-66-NH_2 (Figure 13a), a new energy spectrum peak appears at 576.08 eV after adsorption of Cr (VI). This peak belongs to Cr 2p. The Cr 2p peaks is divided into four peaks (Figure 13b: the two peaks at 577.18 eV and 586.88 eV belong to Cr (III), and the two peaks at 575.88 eV and 585.48 eV belong to Cr (VI)) [32]. The presence of Cr (III) indicates that most of Cr (VI) on the surface of UiO-66-NH_2 is reduced to Cr (III), which indicated that there is a reduction effect during the process of adsorption of Cr (VI) [33].

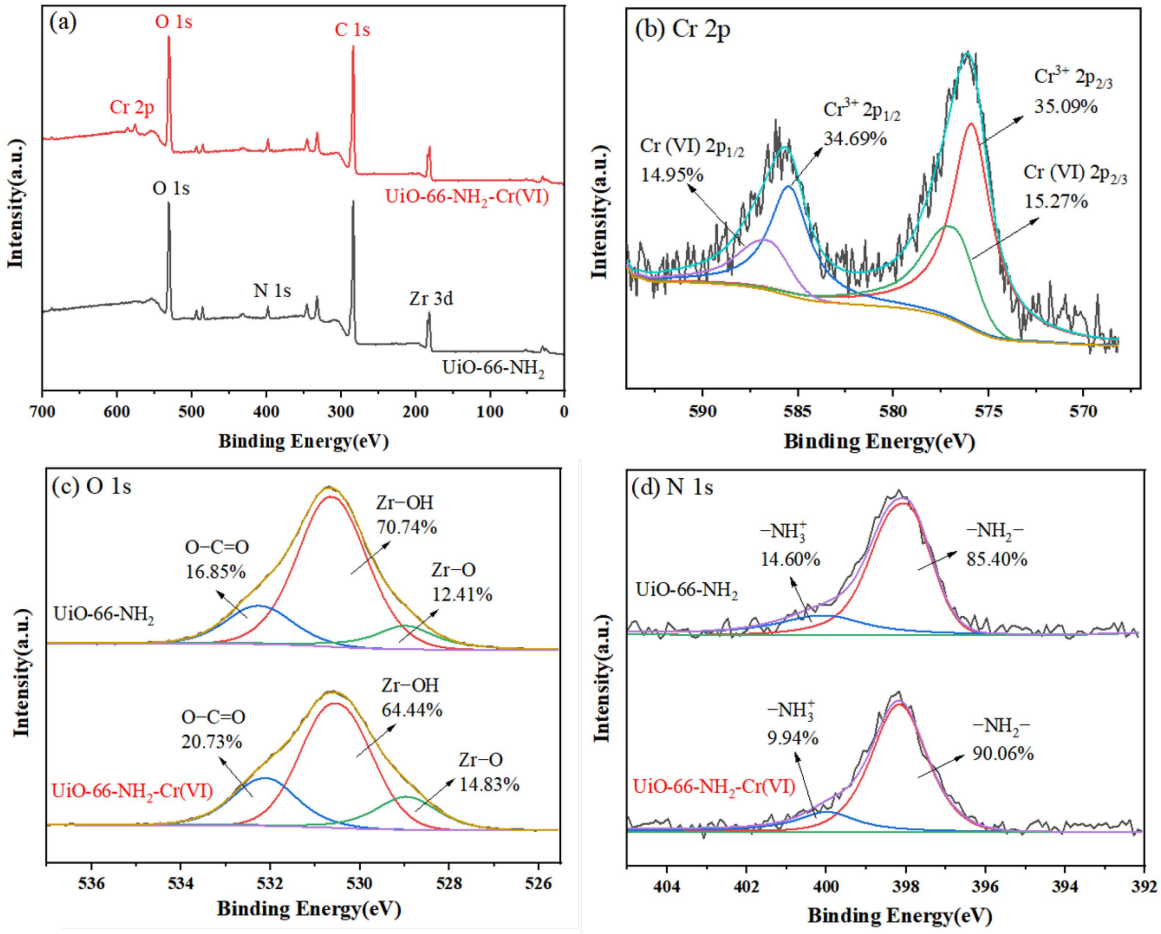

Figure 13. XPS spectra of UiO-66-NH_2 before (**a**) and after (**b**–**d**) adsorption measurement.

The splitting peaks of O 1s before and after adsorption are illustrated in Figure 13c. It can be seen that the peaks before and after adsorption are different. Before adsorption, three peaks were formed at 532.28 (16.85%), 530.68 (70.74%), and 528.98 eV (12.41%), corresponding to O-C=O, Zr-OH, and Zr-O, respectively. After adsorption, the three peaks shifted to a lower binding energy, located at 532.08 (20.73%), 530.58 (64.44%), and 528.98 eV (14.83%), respectively, and the peak area changed. Among them, the energy spectrum peak content of Zr-OH was significantly reduced, indicating that Zr-OH participated in the adsorption process. Thus, there may be a Zr-O-Cr complex between the adsorbent and Cr [34].

The cleavage peaks of N 1s before and after adsorption are shown in Figure 13d. Before adsorption, two peaks were formed at 400.08 eV and 398.08 eV, which were attributed to -NH_2 (85.40%) and -NH_3^+ (14.60%), respectively [35]. After adsorption, the -NH_3^+ peak shifted to a lower binding energy (399.98 eV),) indicating the presence of electrostatic interaction between oxygen atoms (from $HCrO_4-$) and nitrogen atoms (from -NH_3^+ groups). This interaction will induce a slight shift of -NH_2 toward a higher energy (398.18 eV). It can be speculated that there may be electrostatic attraction between -NH_3^+ and Cr (VI). In summary, XPS analysis shows that the adsorption process can be controlled by electrostatic attraction, reduction, and complexation.

4. Conclusions

Under the simple solvothermal method, a UiO-66 formula with high crystallinity and low raw material loss was formed by changing the content of the benzoic acid regulator. Amino functional groups were introduced into UiO-66. With the increase in amino-containing ligands, the crystal size increased, and the edge became more obvious.

When the molar ratio of ligand to zirconium source was 1, the unit adsorption capacity reached the maximum of 305.16 $mg \cdot g^{-1}$. By adding the adsorbent to different acid and alkali environments, it was found that its stability is good and its crystal structure does not collapse. The adsorption conditions of UiO-66-NH_2 for Cr (VI) adsorption were investigated. It can be concluded that when pH = 2 and the content of the adsorbent was 10 mg, the adsorption effect was the best. The adsorption mechanism mainly involves electrostatic attraction, complexation, and reduction processes. After the Cr (VI) stability test, even if stirred in different acid and alkali environments for more than 48 h, Cr (VI) ions are still stable in the adsorbent.

Author Contributions: Conceptualization, Q.L. and Y.W.; software, T.W.; formal analysis, R.Z.; investigation, F.L.; resources, X.H.; data curation, Q.L.; writing—original draft preparation, X.Z. and Q.L.; writing—review and editing, X.Z.; supervision, Y.W.; funding acquisition, Y.W. All authors have read and agreed to the published version of the manuscript.

Funding: This research was funded by the National Natural Science Foundation of China, the Natural Science Foundation of Jiangxi Province of China, and the Key Foundation of Jiangxi Educational Committee grant number (52062021, 20212BAB204034, GJJ211302) and the APC was funded by the National Natural Science Foundation of China, the Natural Science Foundation of Jiangxi Province of China, and the Key Foundation of Jiangxi Educational Committee.

Data Availability Statement: Data will be made available on request.

Acknowledgments: The authors gratefully acknowledge the support of this research by the National Natural Science Foundation of China (Grant No. 52062021), the Natural Science Foundation of Jiangxi Province of China (Grant No. 20212BAB204034), and the Key Foundation of Jiangxi Educational Committee (Grant No. GJJ211302).

Conflicts of Interest: The authors declare that they have no conflicts of interest.

References

1. Yaghi, O.M.; Li, G.; Li, H. Selective binding and removal of guests in a microporous metal–organic framework. *Nature* **1995**, *378*, 703–706. [CrossRef]
2. Zeng, X.; Zhao, Y.; Hu, X.; Stucky, G.D.; Moskovits, M. Rational Component and Structure Design of Noble-Metal Composites for Optical and Catalytic Applications. *Small Struct.* **2021**, *2*, 2000138. [CrossRef]
3. Lin, G.; Zeng, B.; Liu, X.; Li, J.; Zhang, B.; Zhang, L. Enhanced performance of functionalized MOF adsorbents for efficient removal of anthropogenic Hg(II) from water. *J. Clean. Prod.* **2022**, *381*, 134766. [CrossRef]
4. Lee, G.; Park, G.; Kim, S.; Jhung, S.H. Adsorptive removal of aromatic diamines from water using metal-organic frameworks functionalized with a nitro group. *J. Hazard. Mater.* **2023**, *443*, 130133. [CrossRef] [PubMed]
5. Huang, F.; Zhang, X.; Liu, W.; Gao, J.; Sun, L. Theoretical Investigations on MIL-100(M) (M=Cr, Sc, Fe) with High Adsorption Selectivity for Nitrogen and Carbon Dioxide over Methane. *Chem. Asian J.* **2022**, *18*, e202200985. [CrossRef]
6. Yang, P.; Meng, X.; Guo, P.; Zhou, R.; Zhang, Y.; Cao, S.; Zhang, D.; Ji, H.; Duan, L. Highly selective separation of C_3H_6/C_3H_8 within hierarchical metal-organic CuxOy@HP-Cu-BTCs. *Mater. Chem. Phys.* **2023**, *294*, 127024. [CrossRef]
7. Yin, X.; He, Y.; He, T.; Li, H.; Wu, J.; Zhou, L.; Li, S.; Li, C. A durable MOF-303-coated stainless steel mesh with robust anti-oil-fouling performance for multifunctional oil/water separation. *Colloids Surf. A Physicochem. Eng. Asp.* **2023**, *657*, 130515. [CrossRef]
8. Behera, P.; Ray, A.; Tripathy, S.P.; Acharya, L.; Subudhi, S.; Parida, K. ZIF-8 derived porous C, N co-doped ZnO modified B-g-C3N4: A Z-Scheme charge dynamics approach operative towards photocatalytic hydrogen evolution and ciprofloxacin degradation. *J. Photochem. Photobiol. A Chem.* **2023**, *436*, 114415. [CrossRef]
9. Yu, H.; Hong, Y.; Zeng, X.; Wei, J.; Wang, F.; Liu, M. Multilevel reconstruction of g-C_3N_4 nanorings via natural pollen for remarkable photocatalysis. *Mater. Today Sustain.* **2023**, *21*, 100267. [CrossRef]
10. Tan, Y.; Yang, L.; Zhai, D.; Sun, L.; Zhai, S.; Zhou, W.; Wang, X.; Deng, W.-Q.; Wu, H. MXene-Derived Metal-Organic Framework@MXene Heterostructures toward Electrochemical NO Sensing. *Small* **2022**, *18*, 2204942. [CrossRef]
11. Fan, Y.; Li, C.; Liu, X.; Ren, J.; Zhang, Y.; Chi, J.; Wang, L. Honeycomb structured nano MOF for high-performance sodium-ion hybrid capacitor. *Chem. Eng. J.* **2023**, *452*, 139585. [CrossRef]
12. Zeng, X.; Ye, Y.; Wang, Y.; Yu, R.; Moskovits, M.; Stucky, G. Honeycomb-like MXene/NiFePx-NC with "continuous" single-crystal enable high activity and robust durability in electrocatalytic oxygen evolution reactions. *J. Adv. Ceram.* **2023**, *12*, 553–564. [CrossRef]

13. Safinejad, M.; Rigi, A.; Zeraati, M.; Heidary, Z.; Jahani, S.; Chauhan, N.P.S.; Sargazi, G. Lanthanum-based metal organic framework (La-MOF) use of 3,4-dihydroxycinnamic acid as drug delivery system linkers in human breast cancer therapy. *BMC Chem.* **2022**, *16*, 93. [CrossRef]
14. Zeng, X.; Zhao, C.; Nie, T.; Shen, Z.-Y.; Yu, R.; Stucky, G. Construction of 0D/1D/2D MXene nanoribbons-NiCo@NC hierarchical network and their coupling effect on electromagnetic wave absorption. *Mater. Today Phys.* **2022**, *28*, 100888. [CrossRef]
15. Cavka, J.H.; Jakobsen, S.; Olsbye, U.; Guillou, N.; Lamberti, C.; Bordiga, S.; Lillerud, K.P. A New Zirconium Inorganic Building Brick Forming Metal Organic Frameworks with Exceptional Stability. *J. Am. Chem. Soc.* **2008**, *130*, 13850–13851. [CrossRef]
16. Silva, C.G.; Luz, I.; Xamena, F.L.; Corma, A.; García, H. Water Stable Zr-Benzenedicarboxylate Metal-Organic Frameworks as Photocatalysts for Hydrogen Generation. *Chem. Eur. J.* **2010**, *16*, 11133–11138. [CrossRef]
17. Zhang, W.; Yang, J.-M.; Yang, R.-N.; Yang, B.-C.; Quan, S.; Jiang, X. Effect of free carboxylic acid groups in UiO-66 analogues on the adsorption of dyes from water: Plausible mechanisms for adsorption and gate-opening behavior. *J. Mol. Liq.* **2019**, *283*, 160–166. [CrossRef]
18. Xie, H.; Ma, D.; Liu, W.; Chen, Q.; Zhang, Y.; Huang, J.; Zhang, H.; Jin, Z.; Luo, T.; Peng, F.-M. Zr-Based MOFs as new photocatalysts for the rapid reduction of Cr(vi) in water. *New J. Chem.* **2020**, *44*, 7218–7225. [CrossRef]
19. Schaate, A.; Roy, P.; Godt, A.; Lippke, J.; Waltz, F.; Wiebcke, M.; Behrens, P. Modulated Synthesis of Zr-Based Metal-Organic Frameworks: From Nano to Single Crystals. *Chem. A Eur. J.* **2011**, *17*, 6643–6651. [CrossRef]
20. Zhang, A.; Liu, B.; Liu, M.; Xie, Z.; Wang, D.; Feng, G. The adsorption properties of defect controlled metal-organic frameworks of UiO-66. *Sep. Purif. Technol.* **2021**, *270*, 118842. [CrossRef]
21. Wang, Y.; Peng, C.; Jiang, T.; Li, X. Research progress of defect-engineered UiO-66(Zr) MOFs for photocatalytic hydrogen pro-duction. *Front. Energy* **2021**, *15*, 656–666. [CrossRef]
22. Shearer, G.; Chavan, S.; Bordiga, S.; Svelle, S.; Olsbye, U.; Lillerud, K. Defect Engineering: Tuning the Porosity and Compo-sition of the Metal-Organic Framework UiO-66 via Modulated Synthesis. *Chem. Mater.* **2016**, *28*, 3749–3761. [CrossRef]
23. Zhang, X.; Zhang, S.; Ouyang, G.; Han, R. Removal of Cr(VI) from solution using UiO-66-NH2 prepared in a green way. *Korean J. Chem. Eng.* **2022**, *39*, 1839–1849. [CrossRef]
24. Padmavathy, K.; Madhu, G.; Haseena, P. A study on Effects of pH, Adsorbent Dosage, Time, Initial Concentration and Adsorption Isotherm Study for the Removal of Hexavalent Chromium (Cr (VI)) from Wastewater by Magnetite Nanoparticles. *Procedia Technol.* **2016**, *24*, 585–594. [CrossRef]
25. Zhuang, S.; Cheng, R.; Wang, J. Adsorption of diclofenac from aqueous solution using UiO-66-type metal-organic frameworks. *Chem. Eng. J.* **2019**, *359*, 354–362. [CrossRef]
26. Arikawati, E.; Pranoto, T.; Saraswati, E. Preparation of Amine-Functionalized TiO_2/Carbon Photocatalyst by Arc Discharge in Liquid. *IOP Conf. Ser. Mater. Sci. Eng.* **2017**, *176*, 012045. [CrossRef]
27. Prakashbabu, D.; Krishna, R.H.; Nagabhushana, B.; Nagabhushana, H.; Shivakumara, C.; Chakradar, R.; Rama-lingam, H.; Sharma, S.; Chandramohan, R. Low temperature synthesis of pure cubic ZrO_2 nanopowder: Structural and lumi-nescence studies, Spectrochim. *Acta A Mol. Biomol. Spectrosc.* **2014**, *122*, 216–222. [CrossRef]
28. Abdullah, M.; Rajab, F.; Al-Abbas, S. Structural and optical characterization of Cr_2O_3 nanostructures: Evaluation of its dielectric properties. *AIP Adv.* **2014**, *4*, 027121. [CrossRef]
29. Fang, L.; Ding, L.; Ren, W.; Hu, H.; Huang, Y.; Shao, P.; Yang, L.; Shi, H.; Ren, Z.; Han, K.; et al. High exposure effect of the ad-sorption site significantly enhanced the adsorption capacity and removal rate: A case of adsorption of hexavalent chromium by quaternary ammonium polymers (QAPs). *J. Hazard. Mater.* **2021**, *416*, 125829. [CrossRef]
30. Yang, S.; He, D.; Zhang, L.; Zhang, Y.; Lu, J.; Luo, Y. Toxic chromium treatment induce amino-assisted electrostatic adsorption for the synthesis of highly dispersed chromium catalyst. *J. Hazard. Mater.* **2021**, *417*, 126155. [CrossRef]
31. Ma, C.; Zhang, X.; Wen, K.; Wang, R.; Han, R. Facile synthesis of polyethyleneimine@Fe_3O_4 loaded with zirconium for enhanced phosphate adsorption: Performance and adsorption mechanism. *Korean J. Chem. Eng.* **2021**, *38*, 135–143. [CrossRef]
32. Wang, C.; Xiong, C.; He, Y.; Yang, C.; Li, X.; Zheng, J.; Wang, S. Facile preparation of magnetic Zr-MOF for adsorption of Pb(II) and Cr(VI) from water: Adsorption characteristics and mechanisms. *Chem. Eng. J.* **2021**, *415*, 128923. [CrossRef]
33. Xu, C.; Xu, Y.; Zhong, D.; Chang, H.; Mou, J.; Wang, H.; Shen, H. Zr^{4+} cross-linked chitosan-thiourea composite for efficient de-toxification of Cr(VI) ions in aqueous solution. *Carbohydr. Polym.* **2022**, *296*, 119872. [CrossRef]
34. Zhang, Y.; Lan, G.; Liu, Y.; Zhang, T.; Qiu, H.; Li, F.; Yan, J.; Lu, Y. Enhanced adsorption of Cr (VI) from aqueous solution by zir-conium impregnated chitosan microspheres: Mechanism and equilibrium. *Sep. Sci. Technol.* **2021**, *56*, 2532–2545. [CrossRef]
35. Zhang, X.; Liu, M.; Han, R. Adsorption of phosphate on UiO-66-NH2 prepared by a green synthesis method. *J. Environ. Chem. Eng.* **2021**, *9*, 106672. [CrossRef]